applied sciences

Article

Research on the Vibration Behavior of Ring–Block Friction Pair Made of Materials of Water-Lubricated Rubber Bearing under Special Operating Conditions

Zijian Zhang [1], Guangwu Zhou [1,*], Peng Li [1,2], Luole Du [1] and Min He [3]

[1] School of Aeronautics and Astronautics, Sichuan University, Chengdu 610065, China; zzj@stu.scu.edu.cn (Z.Z.); 17629223882@163.com (P.L.); 2021226210009@stu.scu.edu.cn (L.D.)
[2] Xi'an Institute of Electromechanical Information Technology, Xi'an 710065, China
[3] National Institute of Measurement and Testing Technology, Chengdu 610021, China; 15708407422@163.com
* Correspondence: gwzhou@scu.edu.cn

Abstract: A water-lubricated rubber bearing (WLRB) is prone to generate frictional vibration noise under special operating conditions, which seriously affects the acoustic stealth performance of warships and threatens their navigation safety. Meanwhile, the main factor affecting the frictional vibration behavior of a WLRB is the materials of the friction pair. Therefore, this work selects a friction pair composed of a copper ring and a rubber block as the research object and studies the frictional vibration behavior of the ring–block friction pair under low-speed and starting conditions. The real friction coefficient curve is used to establish a transient dynamic finite element analysis model for the ring–block friction pair. The effects of the load, friction coefficient, and Young's modulus on the frictional vibration behavior under special operating conditions are studied. The analysis's results show that the frequency of the medium-high frequency friction-induced vibration disappears under low-speed operating conditions when the friction coefficient is below 0.1. During the startup process, even if the friction coefficient is very low, the medium-high frequency friction-induced vibration still exists. The research results provide ideas for future theoretical research and guidance suggestions for engineering practice.

Keywords: water-lubricated rubber bearing; startup process; friction-induced vibration; real friction coefficient curve

Citation: Zhang, Z.; Zhou, G.; Li, P.; Du, L.; He, M. Research on the Vibration Behavior of Ring–Block Friction Pair Made of Materials of Water-Lubricated Rubber Bearing under Special Operating Conditions. *Appl. Sci.* **2023**, *13*, 7676. https://doi.org/10.3390/app13137676

Academic Editor: Homer Rahnejat

Received: 7 June 2023
Revised: 25 June 2023
Accepted: 26 June 2023
Published: 28 June 2023

1. Introduction

An oil-lubricated bearing carries the risk of lubricating oil leakage, which could pollute seawater quality and harm marine ecosystems. Therefore, researchers are turning their attention to a cleaner and more environmentally friendly water-lubricated rubber bearing (WLRB) [1–3]. A WLRB uses water as a lubricant, which is more environmentally friendly and has better heat dissipation performance than oil. However, at normal temperature and pressure, the viscosity of water is much lower than that of oil, and the smaller viscosity makes the water film bearing capacity of a WLRB much smaller than that of an oil-lubricated bearing [4–6]. Submarines often operate at low speed and with a heavy load, making it difficult to form a water film in the bearing that supports dynamic lubrication, resulting in the bearing having a mixed lubrication or even a dry friction state [7–9]. Rubber, often used as a bearing liner, can generate frictional vibration noise under these conditions, which affects the navigation of warships [10–12]. Therefore, the frictional noise of the WLRB during operation needs to be reduced.

At present, there are several theories to explain the generation of friction noise, which are the stick–slip theory [13,14], mode-coupling theory [15], self-locking-sliding theory [16], and friction-negative slope of the relative sliding velocity curve theory [17]. In the field of noise in WLRBs, researchers also conducted a lot of scientific research work [18–21]. As early as the 1990s, Simpson [22] proposed the nonlinear variation of the friction coefficient, laying the foundation for the theory of the friction-negative slope of the relative sliding velocity curve by later generations. Dong [23] studied the stick–slip behavior of polymer materials under water lubrication and low-speed conditions on a friction testing machine and found that the speed affects deformation and, thus, stick–slip. Liu [24] used a disk-slider to study the stick–slip vibration characteristics and found that the change in the disk speed has a significant impact on the vibration. Therefore, when studying the vibration characteristics, it is necessary to consider the time-varying velocity. Kuang [25] studied the mechanism and process of the friction-induced vibration and torsional vibration coupling and visually displayed the coupling process of the friction-induced vibration and torsional vibration in the tailshaft system. When the engine is in the starting state, the WLRB is in both a low-speed state and a speed time-varying state. Based on the above research status, the vibration is affected by multiple factors at this time, so it is necessary to analyze the vibration situation during startup.

The traditional way to study the frictional vibration behavior of the WLRB is through experiments [26–28]. With the development of finite element software, many researchers began to use finite element software to analyze the frictional vibration behavior. Scholars initially studied the braking noise of friction brake discs. For example, Balaji [29] conducted a complex modal analysis of disc brakes using ABAQUS and found that reducing the friction coefficient and increasing the stiffness of the friction disc can reduce the vibration frequency of the friction noise. Chen [30] used complex mode analysis and transient dynamics in ABAQUS to study the vibration behavior between metal sliding blocks and found that the vibration frequency is very sensitive to the sliding speed and contact pressure. Chen also showed the time-varying contact pressure between the sliding blocks, indicating that the jumping of the sliding blocks is the main source of noise, which revealed a new mechanism of the noise source and laid the foundation for future research. Thi-Na [31] used finite element software to analyze the resonance frequency of a four-ball wear testing machine and analyzed the correlation between the lubricant and friction coefficient.

Many scholars used complex modal methods to study the frictional vibration behavior of the WLRB, but this method cannot consider nonlinear problems. Transient dynamics can consider nonlinear problems, but when scholars used transient dynamics for research, they did not consider the time-varying friction coefficient during the startup process and mostly analyzed the steady-state vibration situation. Transient dynamics could consider nonlinear problems, but scholars did not consider the time-varying friction coefficient during the startup process when using transient dynamics for research. Scholars mostly analyzed the vibration situation in the steady state. However, it is difficult to form a lubricating water film during low-speed operating conditions and startup processes. The friction pair is in a mixed lubrication state or even a dry friction state, and the friction coefficient has time-varying characteristics, which are significantly different from the high-speed steady-state operating conditions. The time-varying characteristics of the speed and the friction coefficient have a significant impact on vibration [23,24]. However, only a few articles considered the time-varying friction coefficient [32]. In this article, finite element software was used to simulate the parking process by defining the relationship between the friction coefficient of the contact pair and the speed, and the effects of parameters such as the friction coefficient, specific pressure, and temperature on the vibration behavior of the WLRB were analyzed.

The main factor affecting the friction-induced vibration behavior of a WLRB is the materials, so a ring–block friction pair experiment is undoubtedly an excellent experiment for determining the materials' selection. Therefore, this article uses a ring–block to replace the friction system in a WLRB, measuring the real friction coefficient curve and the speed loading curve through pretests. The influence of different parameter changes on the friction-induced vibration behavior during low-speed operating conditions and startup processes is studied, which has significant research significance for better understanding the vibration and noise behavior of friction pairs. It has practical engineering significance for guiding the materials' selection and material modification design of water-lubricated rubber bearing pads.

2. Analysis Model and Experimental Verification

2.1. Fundamentals of Dynamics Theory

In Abaqus nonlinear dynamics analysis, both explicit dynamics and implicit dynamics can solve for the acceleration of each node, achieving balance between force and node acceleration. The equations of motion of the friction system can be written as Equation (1).

$$[\mathrm{M}]\ddot{x} = \mathrm{F} - \mathrm{P} \tag{1}$$

In the equation: $[\mathrm{M}]$ stands for mass matrix; P stands for the internal force acting on the structure; F stands for the external force on the structure.

In Equation (1), the actual equilibrium equation is replaced by an implicit integration operator of the weight of the inertial force at the end of the time step and the weighted average of the static force at the beginning of the time step, resulting in

$$\mathrm{M}\ddot{x}_{(\mathrm{t}+\Delta\mathrm{t})} - (1+\alpha)\left(\mathrm{F}_{(\mathrm{t}+\Delta\mathrm{t})} - \mathrm{P}_{(\mathrm{t}+\Delta\mathrm{t})}\right) + \alpha(\mathrm{F}_{\mathrm{t}} - \mathrm{P}_{\mathrm{t}}) = 0 \tag{2}$$

In the Newmark method [33], the displacement and velocity of the system can be expressed as

$$x_{(t+\Delta t)} = x_t + \Delta t \cdot \dot{x}_t + \Delta t^2\left(\left(\frac{1}{2} - \beta\right)\ddot{x}_t + \beta\ddot{x}_{t+\Delta t}\right) \tag{3}$$

$$\dot{\mathrm{x}}_{(\mathrm{t}+\Delta\mathrm{t})} = \dot{\mathrm{x}}_{\mathrm{t}} + \Delta\mathrm{t}((1-\gamma)\ddot{\mathrm{x}}_{\mathrm{t}} + \gamma\ddot{\mathrm{x}}_{\mathrm{t}+\Delta\mathrm{t}}) \tag{4}$$

In the equation: $\beta = \frac{1-\alpha^2}{4}$, $\gamma = \frac{1}{2} - \alpha$, $-\frac{1}{3} \leq \alpha \leq 0$.

The implicit time integration method uses automatic incremental steps to iteratively solve using the Newton method. At the end of the incremental step of time "t + Δt" analysis, Newton iteration calculates the displacement at this time.

2.2. Construction of Ring–Block Friction Pair Model

The research object of this article is the friction pair composed of copper ring and rubber block. The size of the copper ring has an outer diameter of 35 mm and a width of 10 mm. The rubber block is assembled from nitrile rubber block and 45 carbon steel block. The rubber is fixed on the steel block through vulcanization, and the clamp clamps the steel block for loading. The rubber block size is 16 mm × 6.5 mm × 6.5 mm, and the steel block size is 16 mm × 6.5 mm × 6 mm. In addition, the finite element model is established, as shown in Figure 1.

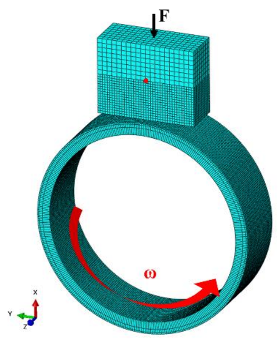

Figure 1. Ring–block finite element model.

Materials: The rubber block is mainly under pressure in this experiment, and the stress–strain curve of the rubber is measured using the CMT5305 electronic universal testing machine before the experiment. In the rubber compression test, it is found that the rubber is in the linear deformation stage, so the Young's modulus of the rubber is directly calculated, which is 13.71 MPa. The parameters of each material are shown in Table 1.

Table 1. Material parameters.

Material	Density (kg·m^{-3})	Young's Modulus (MPa)	Poisson's Ratio
Copper	8900	106,000	0.35
Rubber	1271	13.71	0.47
45 carbon steel	7800	206,000	0.3

Meshing: The rubber part adopts C3D8H hexahedral elements, and the number of elements for the rubber block is 5408. The metal part adopts C3D8R hexahedral units, with 672 steel block units and 12,000 copper ring units. After 100% mesh refinement, the model has a total of 46,080 meshes, but the difference in results is only 0.032%. An example analysis requires 10 h and 11 min for model with 18,080 meshes but 27 h and 2 min for model with 46,080 meshes, and the computer configuration is shown in Table 2. Therefore, in order to accelerate computing speed, the model with 18,080 meshes is used.

Table 2. Computer configuration.

Case	Configuration
CPU	Intel (R) Core (TM) i7-9700
GPU	NVIDIA GeForce GTX 1660 Ti
RAM	DDR4 16 G (8 G × 2)

Boundary conditions: In finite element analysis, the accuracy of the obtained results is closely related to the accuracy of the set boundary conditions. In this model, the copper ring is coupled to its center point, with a fixed constraint applied to the center point, and a speed load of 50 rpm is also applied to this point. The upper surface of the steel block is coupled with its center point, and displacement constraints are set at the center point to constrain the five degrees of freedom of the steel block, only allowing vertical movement of the steel block, that is, only x-axis degrees of freedom exist. A vertical load of 50 N is applied to the center point of the surface of the steel block. Tie constraints are used between the upper surface of the rubber block and the lower surface of the steel block. Penalty contact is used between the lower surface of the rubber and the outer surface of the copper ring, and the specific friction coefficient is obtained through experiments in subsequent chapters and written into the model.

Analysis step: The vibration frequency of water-lubricated bearings in existing articles is around 2000 Hz [8]. So the analysis step length is set to 1 s, and the field output and process output are output 6000 times within 1 s, which means the vibration frequency that can be analyzed is 3000 Hz. The process output is the acceleration time curve along the y-axis at the red point in Figure 1, in order to analyze the vibration of the rubber block.

2.3. Friction Coefficient Curve for Special Operating Conditions

In the analysis process of finite element software, the contact problem is the most important part of the entire process. In the past, the finite element analysis of the vibration behavior of WLRB is mostly steady-state, and the friction coefficient is a stable value that does not change. However, in the real process of initiation, the friction coefficient is time-varying, is strongly related to factors such as rotational speed, and has a strong impact on vibration behavior. During the startup process of WLRB, the rotational speed is too low to form a dynamic pressure water film. The friction state is mixed lubrication or even dry friction, with a large friction coefficient, and the frictional vibration behavior is also significantly different from that of the stable operation of the bearing. The friction coefficient in this article is measured through experiments and correlates with the rotational speed, which also ensures the authenticity and accuracy of the finite element analysis.

The pretest consists of two parts. The first part is to acquire the friction coefficient under low-speed operating conditions. The second part is to acquire the friction coefficient and rotational speed loading curve during the startup process. UMT-TriboLab friction and wear testing machine is used to conduct preliminary experiments, as shown in Figure 2.

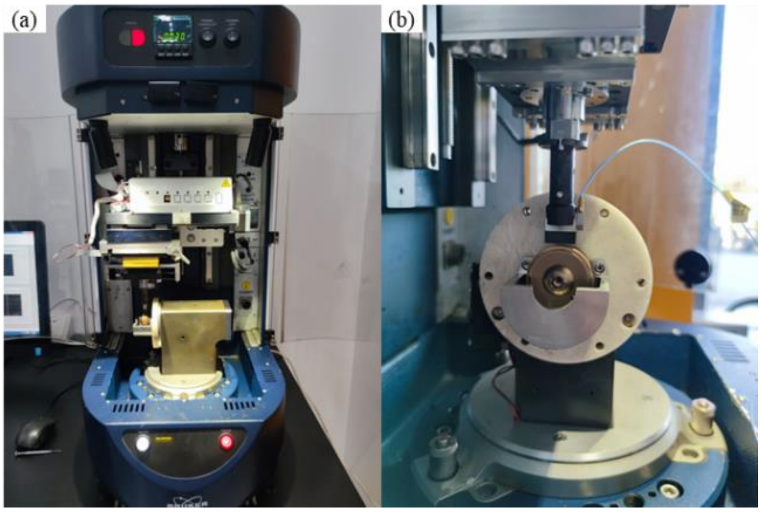

Figure 2. Photos of test device: (**a**) UMT-TriboLab; (**b**) test placement.

The step of the low-speed operating condition pretest is to apply a load of 50 N to the block and apply a rotational speed of 50 rpm (linear speed of about 0.09 m·s^{-2}). Friction coefficient curve is extracted within 4 s after the friction coefficient stabilizes, as shown in Figure 3. As can be seen from Figure 3, the friction coefficient is stable around 0.15, and, in the subsequent analysis, the friction coefficient for low-speed operating condition is set to 0.15.

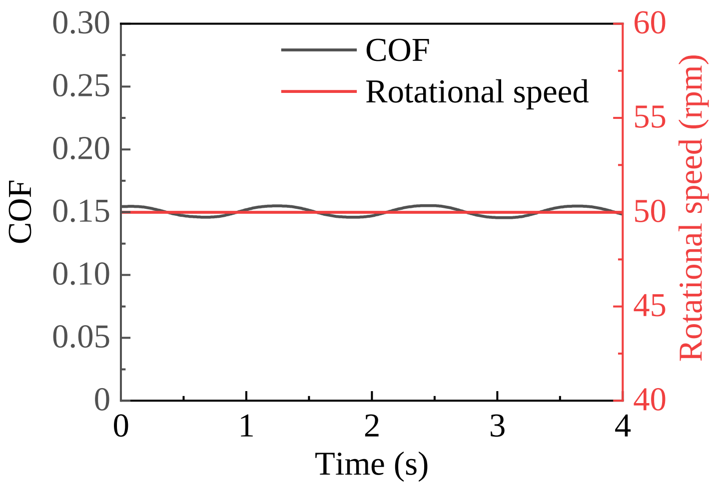

Figure 3. COF curve and speed loading curve of low-speed operating condition.

The pre-experimental step of the startup process is to apply a load of 50 N to the block and apply a rotational speed of 216 rpm (linear speed of about 0.4 m·s^{-2}). The friction coefficient curve and speed curve are extracted within 1 s of startup process, as shown in Figure 4. The obtained friction coefficient curve and speed curve are written into the software for subsequent calculations.

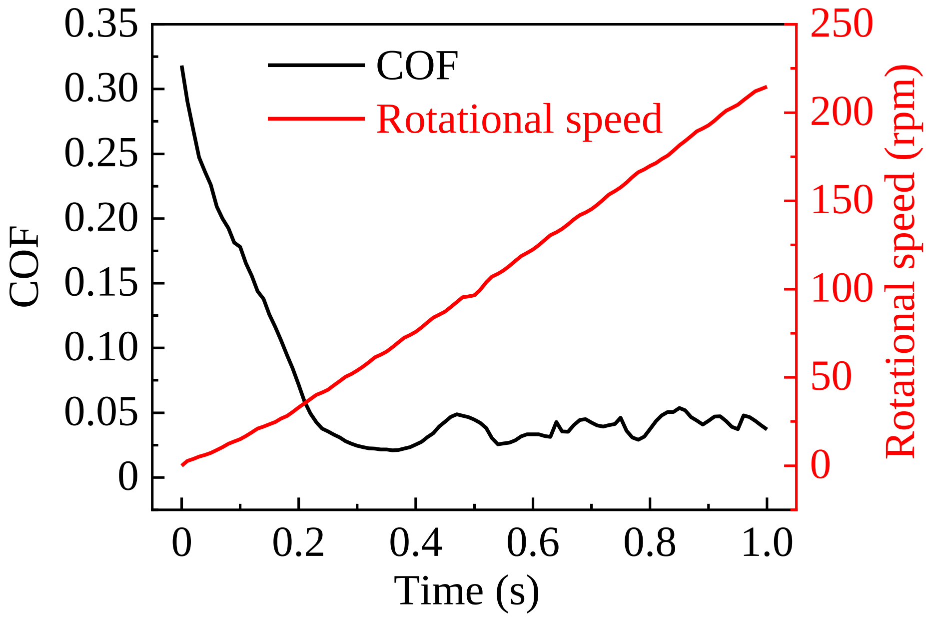

Figure 4. COF curve and speed loading curve of startup process.

2.4. Validation Experiment

The accuracy of the model should be verified before analyzing the model. The analysis results of the vibration model of the ring block friction pair established in the previous section are shown in Figure 5. Figure 5a shows the low-speed operating condition vibration time-domain diagram extracted from the finite element software, and Figure 5b shows the startup process vibration time-domain diagram extracted from the finite element software.

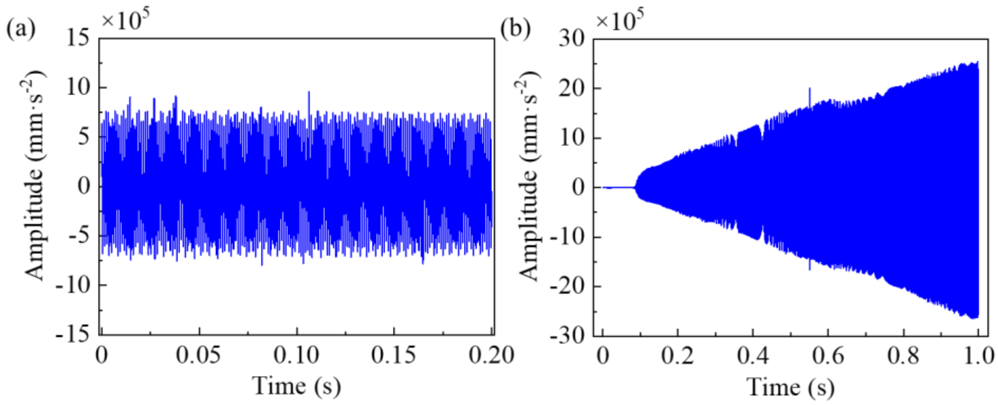

Figure 5. Vibration time-domain diagram: (**a**) low-speed operating condition; (**b**) startup process.

The validation experiment for loading is conducted using the UMT-TriboLab friction and wear testing machine (Figure 2a), and the Donghua 5922D dynamic signal testing and analysis system is used for data collection. The block is fixed onto the testing machine through a fixture, and the acceleration sensor obtains the acceleration signal during vibration by adsorbing it onto the fixture (Figure 2b).

The validation experiment is also divided into two parts, which verify the accuracy of the low-speed operating condition and the startup process model. The first step is to validate the finite element model under low-speed operating condition. The machine applies a radial load of 50 N to the block, followed by a rotational speed of 50 rpm to the ring. The vibration data in the experiment are obtained through an acceleration sensor. Figure 6a shows the background noise signal, in which noisy signals already appear. These signals are caused by internal vibration during operation of the testing machine after loading. Figure 6b shows the vibration noise signal. Compared with the background noise signal and the vibration noise signal, only new vibration noise signals appeared between 1500–2000 Hz (in the blue shading shown in Figure 6a,b), while the remaining signals can be considered as amplified signals of the background signal after loading the speed. By performing bandpass filtering on the vibration noise signal, the frequency domain diagram in Figure 6c is obtained. From Figure 6c, it can be seen that the peak frequency is 1785.2 Hz, which is considered as a frictional vibration signal of the interaction between the ring and block. Similarly, the frequency domain map extracted by finite element software is used for bandpass filtering to obtain the frequency domain map shown in Figure 6d. Through verification, the error of the low-speed operating condition finite element model is only 0.16%.

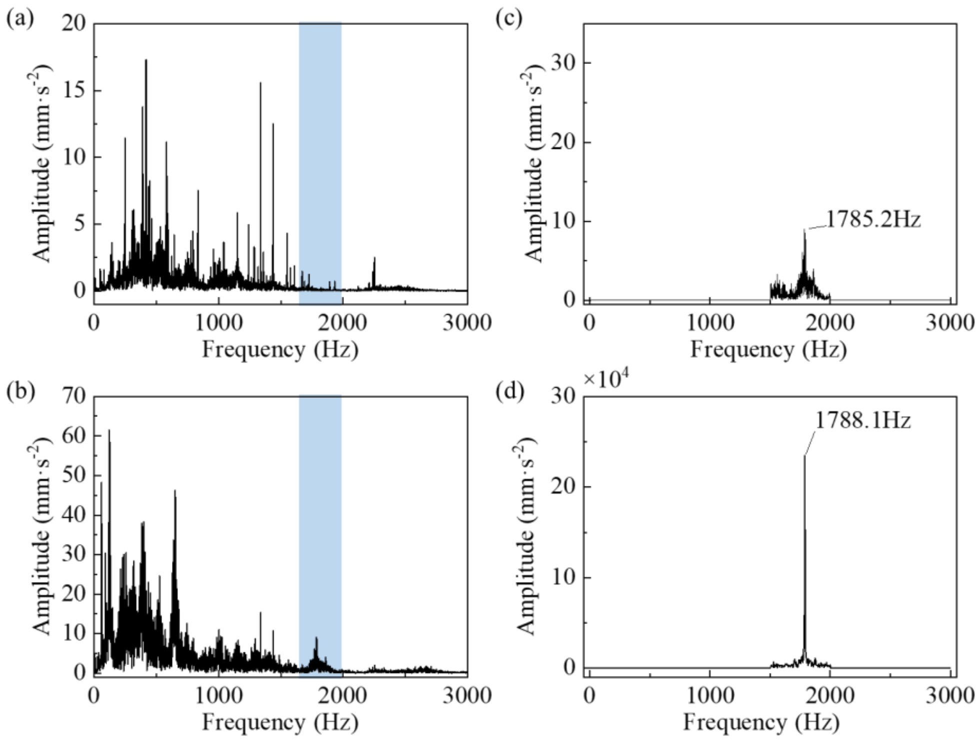

Figure 6. Verification results of low-speed operating condition: (**a**) background noise signal; (**b**) vibration noise signal; (**c**) experimental vibration noise signal after bandpass filtering; (**d**) analyzed vibration noise signal after bandpass filtering.

The second step is to validate the finite element model of the startup process. The machine applies a radial load of 50 N to the block, followed by a rotational speed of 216 rpm applied to the ring. The verification process is similar to that previously described (Figure 7). Through verification, the error of the finite element model is only 3.16%.

After verification, the error of the finite element model analysis results for low-speed operating condition and startup process is 0.16% and 3.16%, respectively. So it is believed that the model is accurate and reliable, and it is used to conduct subsequent factor impact analysis.

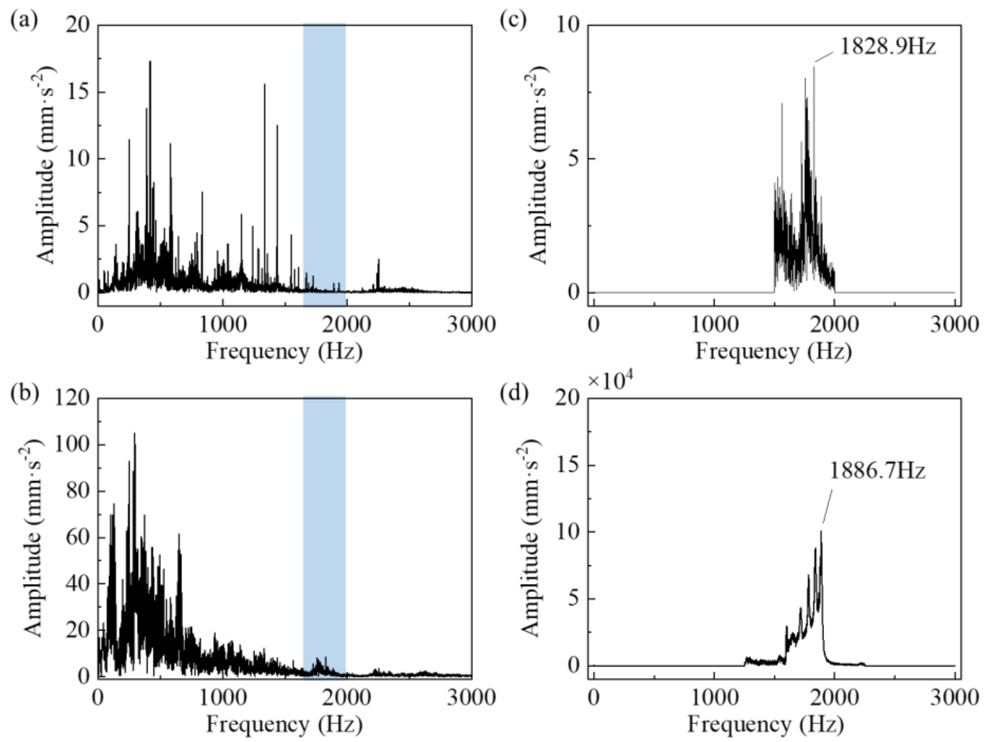

Figure 7. Verification results of startup process: (**a**) background noise signal; (**b**) vibration noise signal; (**c**) experimental vibration noise signal after bandpass filtering; (**d**) analyzed vibration noise signal after bandpass filtering.

3. Friction-Induced Vibration Behavior under Low-Speed Operating Conditions

The frictional vibration behavior of a WLRB under the low-speed operating condition is influenced by various factors. This section uses the transient dynamic model established earlier to analyze the effects of the load, the friction coefficient, and the rubber's Young's modulus on the vibration behavior of ring–block friction pairs under low-speed operating conditions. Based on the obtained results, it can provide guidance and suggestions for theoretical design.

3.1. Effect of Load on Frictional Vibration Behavior

The load is a key factor that affects the vibration behavior of the WLRB, and this section analyzes the influence of the load. While keeping the other factors constant, only the load is changed for analysis. Figure 8 is a time-domain and frequency-domain diagram of the load at 30, 40, 50, 60, and 70 N. In addition, the displacement of the steel block is extracted under different loads, and the curve is plotted, as shown in Figure 9.

The load increases from 30 N to 70 N, and the peak frequency increases from 1708.6 Hz to 1828.4, respectively, an increase of 7.01%. The displacement of the steel block increases from 0.320 mm to 0.575 mm, an increase of 79.7%, as shown in Figure 9.

The contact area of the friction pair is a significant factor affecting the vibration behavior. Rubber is a low-modulus elastic material, which is different from high-modulus metal materials. When the load increases, the rubber undergoes significant deformation due to its smaller modulus. This greatly increases the contact area, thereby affecting the frictional vibration behavior. Additionally, the rise in the applied load results in a surge of friction and contact pressure, ultimately elevating the internal stress and deformation of the bearing and intensifying the level of the frictional oscillation [34,35].

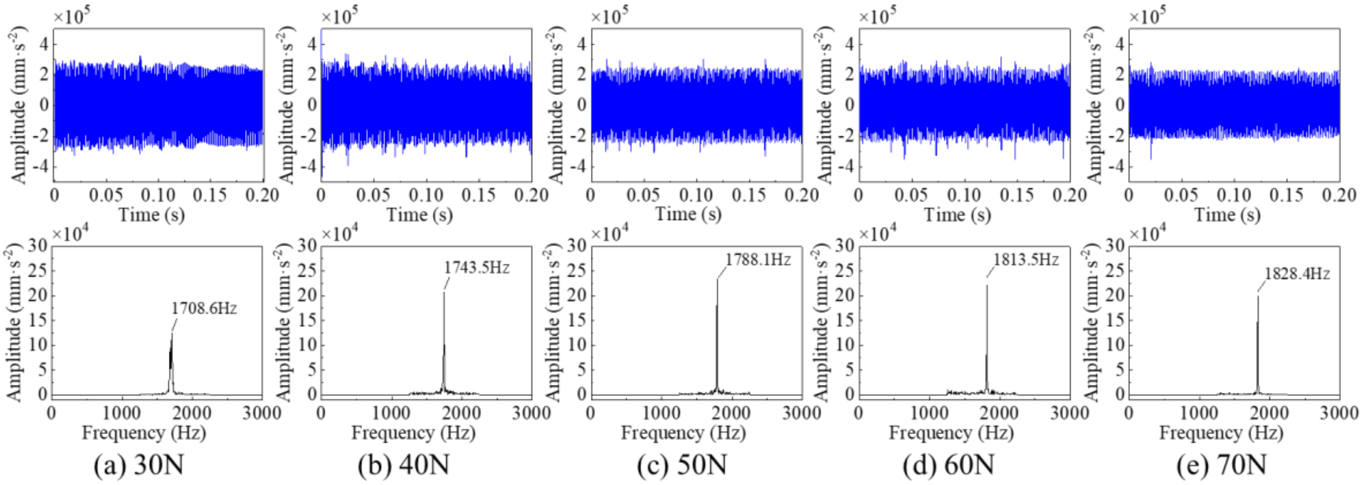

Figure 8. Time-domain and frequency-domain diagrams of low-speed operating condition under different loads.

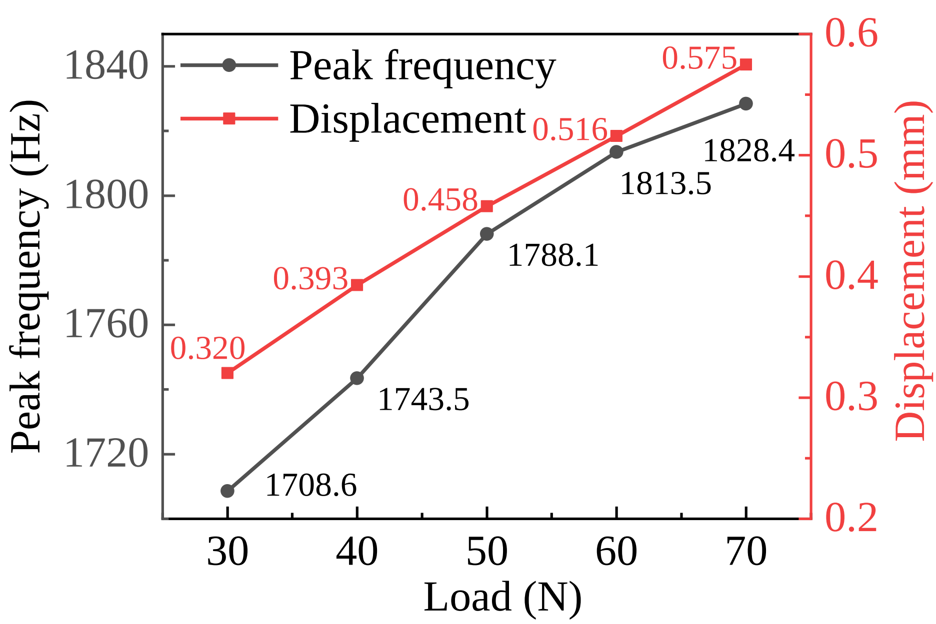

Figure 9. Peak frequency and downforce displacement of low-speed operating condition under different loads.

3.2. Effect of Friction Coefficient on Frictional Vibration Behavior

The friction coefficient is the ratio of the frictional force to the positive pressure on the surface of two objects. The higher the coefficient of friction is, the greater the frictional force is. The change in friction coefficient directly affects the frictional vibration behavior.

In this section, the frictional vibration behavior of ring–block friction pairs under different friction coefficients is analyzed. The initial friction coefficient is set to f_0 ($f_0 = 0.15$). f_0 is multiplied by different coefficients to obtain friction coefficients from 0.5 f_0 to 1.5 f_0. The obtained friction coefficient is substituted into finite element software for analysis.

Figure 10a–e show the time-domain and frequency-domain diagrams of the frictional vibration under the low-speed operating condition, with five sets of friction coefficients ranging from 0.5 f_0 to 1.5 f_0. During the process of increasing the friction coefficient from 0.75 f_0 to 1.5 f_0, the peak frequency of the friction-induced vibration increases from 1738.5 Hz to 1818.5 Hz, respectively, an increase of about 4.60%, as shown in Figure 11.

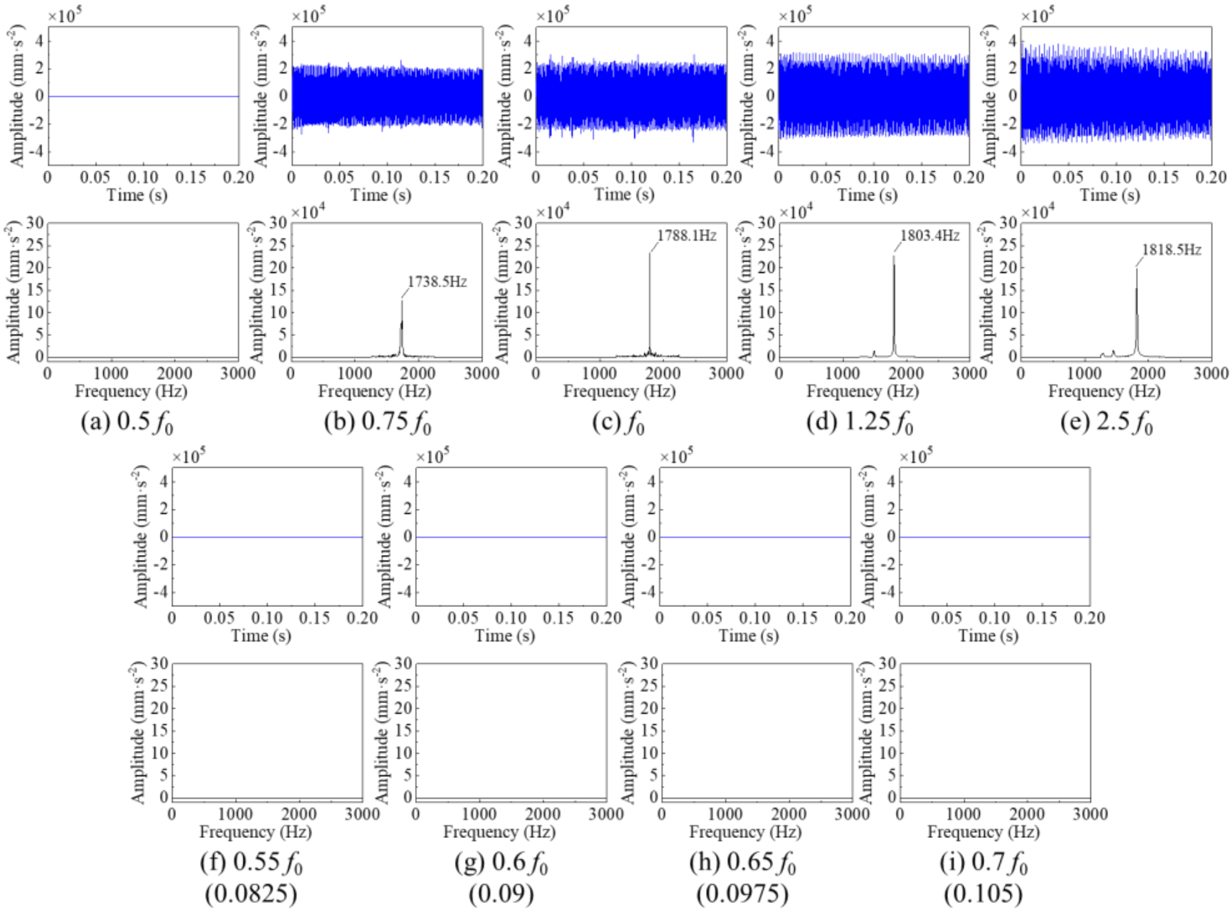

Figure 10. Time-domain and frequency-domain diagrams of low-speed operating conditions under different COFs.

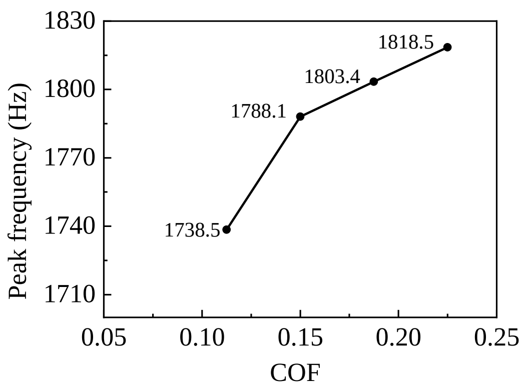

Figure 11. Peak frequency of low-speed operating conditions under different COFs.

However, in the analysis of 0.5 f_0, the friction-induced vibration frequency at medium-high frequencies disappears. Subsequently, finer grouping is carried out between 0.5 f_0 and 0.75 f_0, and the four finer groups also do not have medium-high frequency frequencies, as shown in Figure 10f–i. Among these four groups, the highest friction coefficient is 0.7 f_0, which corresponds to a friction coefficient of 0.105. Therefore, it is believed that when the friction coefficient is below 0.1, the vibration behavior of the friction pair is excellent. In engineering practice, the friction coefficient under low-speed conditions should also be reduced to below 0.1.

3.3. Effect of Young's Modulus on Frictional Vibration Behavior

In engineering practice, rubber with a different hardness is usually used as the bearing lining. Rubber with a different hardness has a different Young's modulus, and the frictional vibration behavior also changes with the change in the Young's modulus. So this section analyzes the influence of the Young's modulus on the frictional vibration behavior under low-speed operating conditions. The initial Young's modulus is set as E_0 (E_0 = 13.71 MPa), and E_0 is multiplied by different coefficients to obtain five Young's moduli: 0.5 E_0, 0.75 E_0, E_0, 1.25 E_0, and 1.5 E_0. The obtained Young's modulus is substituted into finite element software for analysis.

Figure 12 shows the time-domain and frequency-domain diagrams of the frictional vibration under low-speed operating conditions with five Young's moduli. From 0.5 E_0 to 1.5 E_0, the peak frequency increases from 1443.8 Hz to 1928.4 Hz, respectively, an increase of approximately 33.6%. The downward displacement of the steel block decreased from 0.762 mm to 0.346 mm, a reduction of 52.3%, as shown in Figure 13.

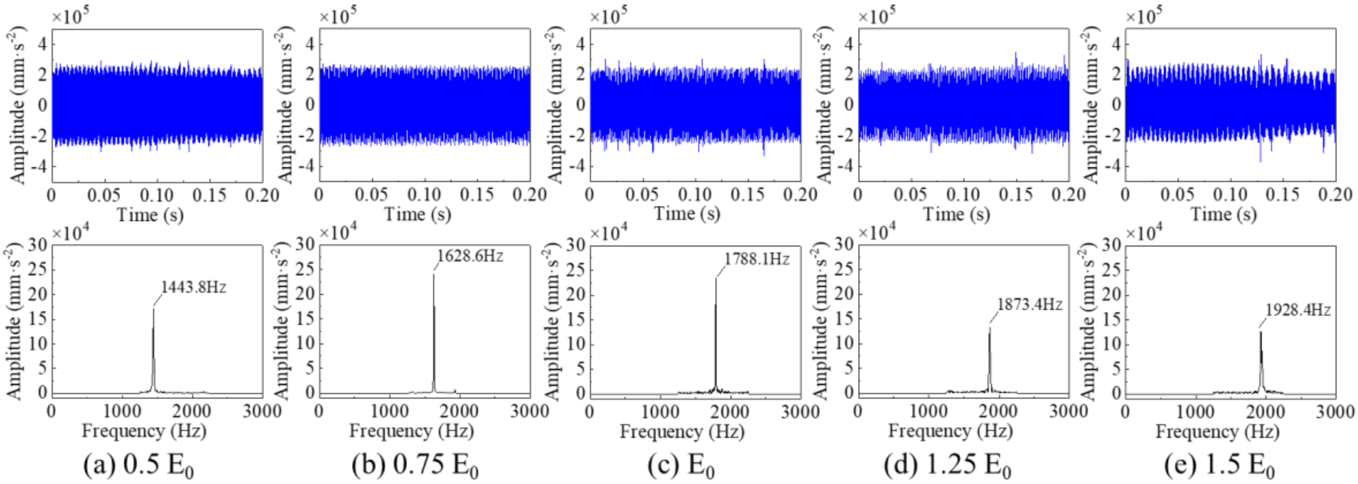

Figure 12. Time-domain and frequency-domain diagrams of low-speed operating conditions under different Young's moduli.

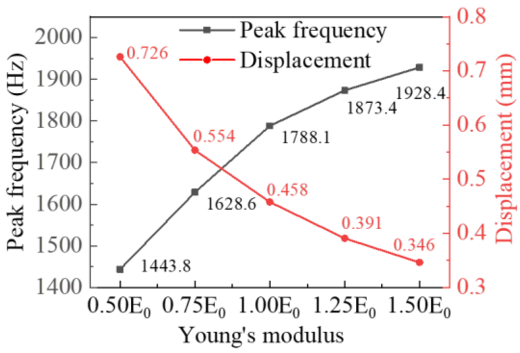

Figure 13. Peak frequency and downforce displacement of low-speed operating conditions under different Young's moduli.

The modulus of the materials directly affects the frictional vibration behavior of objects. The modulus also affects the displacement of the block, thereby indirectly affecting the frictional vibration behavior by affecting the contact area between the ring and the block. The modulus can also affect the bearing capacity, with a large modulus indicating a strong bearing capacity, and vice versa. In engineering design, selecting low-modulus materials to reduce the vibration frequency can also lead to a decrease in the load-bearing capacity. Therefore, comprehensive consideration should be given, between the vibration behavior and the load-bearing capacity, to select the most suitable material.

4. Friction-Induced Vibration Behavior under Startup Processes

The frictional vibration behavior of a WLRB during the startup process is influenced by various factors. This section uses the transient dynamic model established earlier to analyze the effects of the load, the friction coefficient, and the rubber's Young's modulus on the vibration behavior of the ring–block friction pair during startup, based on the obtained results, which can provide guidance and suggestions for theoretical design.

4.1. Effect of Load on Frictional Vibration Behavior

While keeping the other variables constant, only the load is changed to analyze the impact of the load on the frictional vibration behavior during the startup process. Figure 14 is a time-domain and frequency-domain diagram of the load at 30, 40, 50, 60, and 70 N. In addition, the displacement of the steel block is extracted under different loads, and the curve is plotted, as shown in Figure 15.

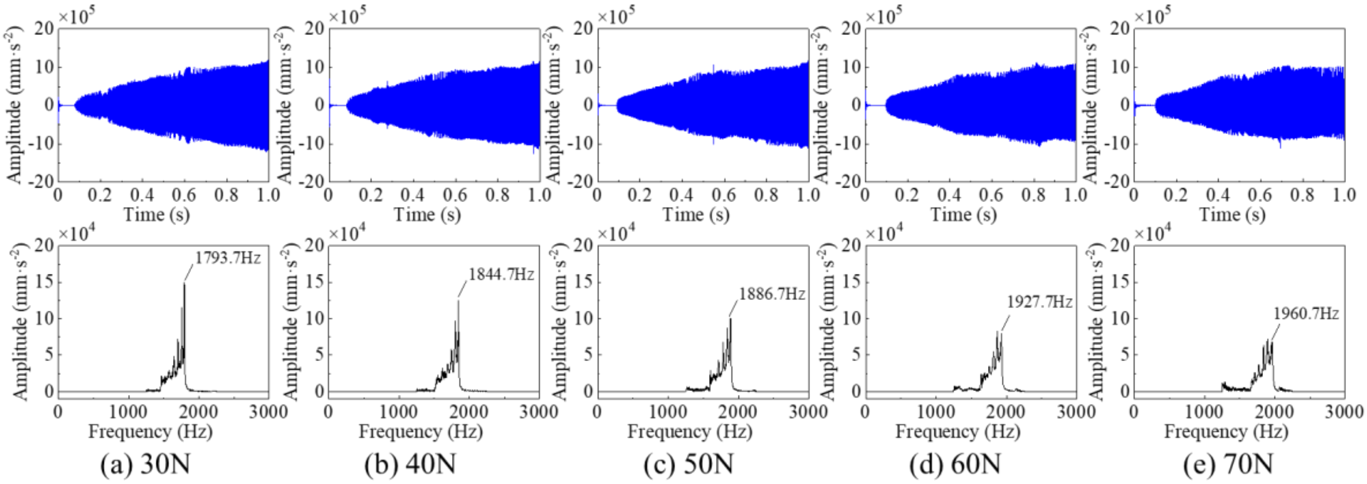

Figure 14. Time-domain and frequency-domain diagrams of startup process under different loads.

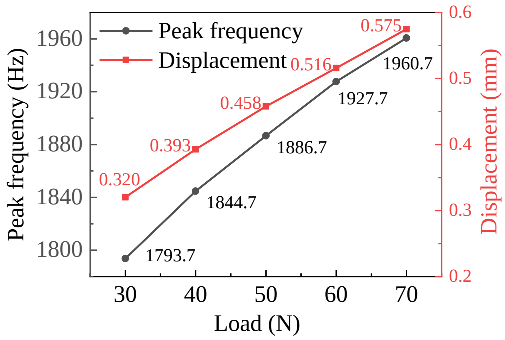

Figure 15. Peak frequency and downforce displacement of startup process under different loads.

The load increases from 30 N to 70 N, and the peak frequency increases from 1793.7 Hz to 1960.7 Hz, respectively, an increase of 9.31%. In addition, the load increases from 30 N to 70 N, and the displacement of the steel block increases from 0.320 mm to 0.575 mm, respectively, an increase of 79.7%.

Similar to the previous low-speed operating conditions, the rise in the applied load leads to an increase in factors such as stress and the contact area of the friction pair, resulting in an increase in the frictional vibration frequency. However, the friction-induced vibration frequency during the startup process is higher than that under low-speed operating conditions under the same load. For instance, in the case of 50 N, the frequency of the startup process is 5.5% higher. This is because the constantly increasing rotational speed and the time-varying friction coefficient during the startup process result in more intense and complex frictional vibrations. This also results in a higher frequency of the frictional vibration during the startup process.

4.2. Effect of Friction Coefficient on Frictional Vibration Behavior

This article analyzes the frictional vibration behavior of the ring–block friction pair during the startup process under different friction coefficients. Setting the friction coefficient curve in Figure 3 as f_0, f_0 is multiplied by different coefficients to obtain five different sets of friction coefficient curves, namely, 0.5 f_0, 1.5 f_0, 2 f_0, 2.5 f_0, and 3 f_0, as shown in Figure 16. Then, the obtained friction coefficient curve is written into finite element software for analysis using keywords.

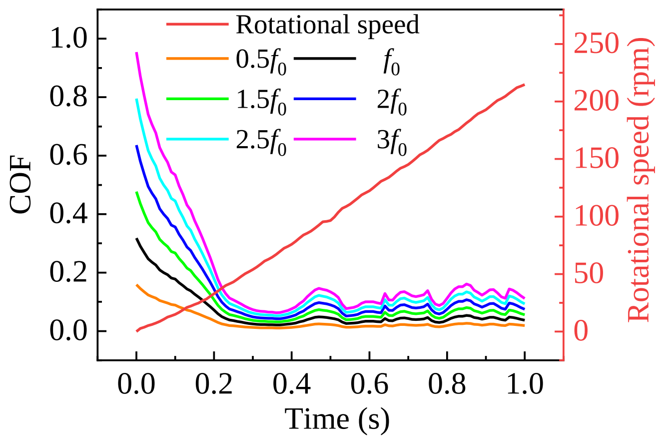

Figure 16. Five sets of friction coefficient curves and rotational speed loading curves.

Figure 17 shows the time-domain and frequency-domain diagrams of the frictional vibration during the startup process under five sets of friction coefficients ranging from 0.5 f_0 to 3 f_0. During the process of increasing the friction coefficient from 0.5 f_0 to 3 f_0, the peak frequency of the friction-induced vibration increases from 1881.7 Hz to 1903.7 Hz, an increase of approximately 1.17%, as shown in Figure 18.

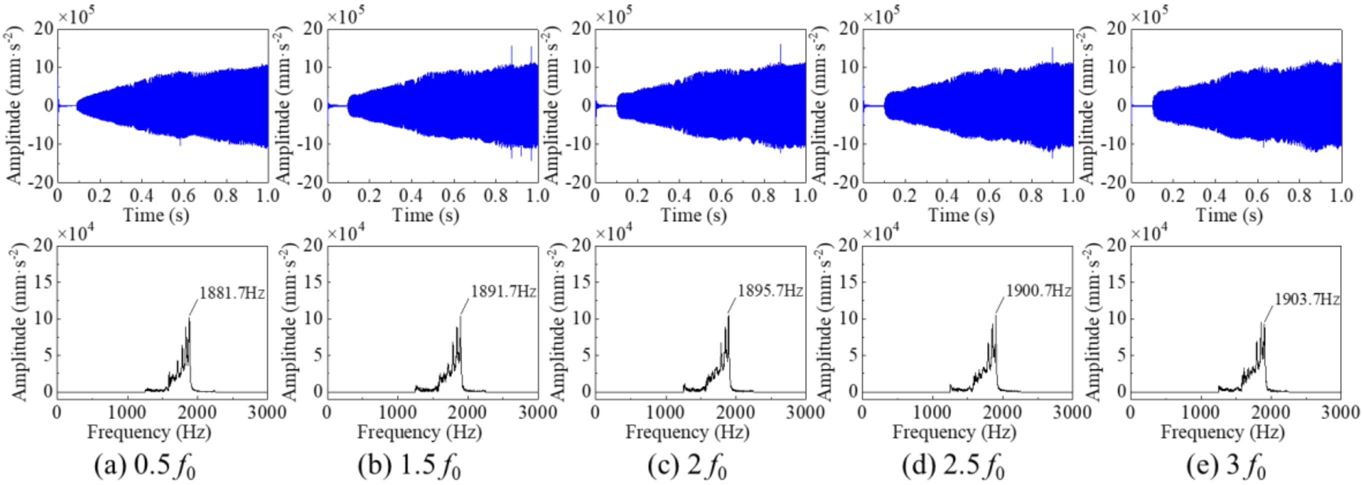

Figure 17. Time-domain and frequency-domain diagrams of startup process under different COFs.

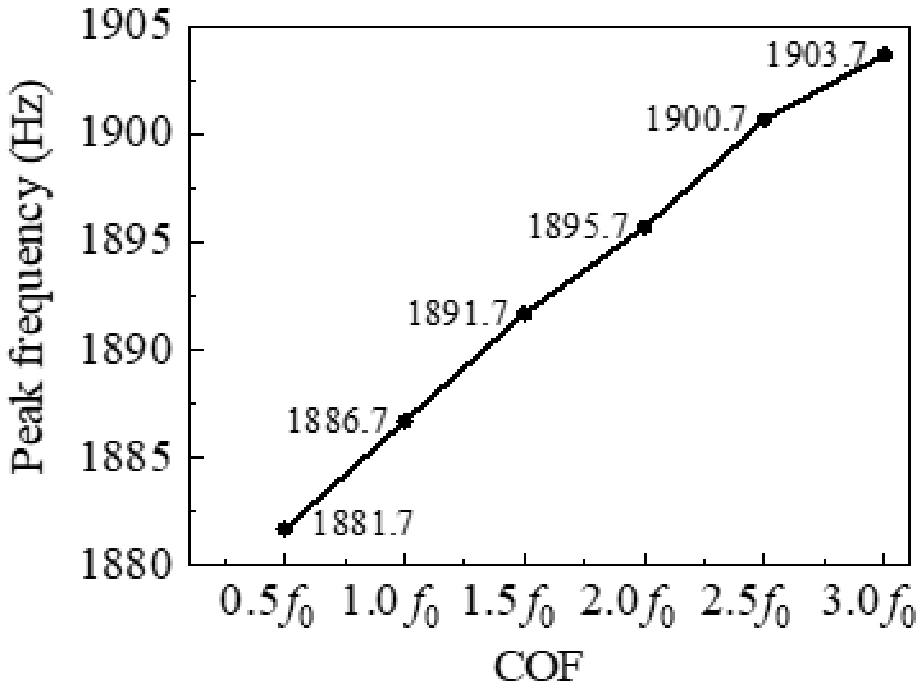

Figure 18. Peak frequency and downforce displacement of startup process under different COFs.

In the previous analysis, the frequency of the medium-high frequency friction-induced vibration disappears under the low-speed operating condition when the friction coefficient is below 0.1, and the friction-induced vibration behavior is excellent. From Figure 16, it can be seen that after 0.3 s, the friction coefficient basically drops below 0.1. The friction coefficient of 0.5 f_0 fluctuates around 0.02 after 0.3 s, much lower than the 0.1 mentioned earlier. However, at this point, the medium-high frequency vibration frequency still exists. Therefore, it is believed that the increase in the rotational speed and the time-varying friction coefficient have a comprehensive impact on the generation of medium-high frequency friction-induced vibrations. In future analysis, the vibration behavior corresponding to a certain rotational speed during the startup process cannot be equated with the vibration behavior corresponding to a certain rotational speed in the steady state. An analysis should consider the impact of time-varying velocity on vibration behavior.

4.3. Effect of Young's Modulus on Frictional Vibration Behavior

This section analyzes the effect of the Young's modulus on the frictional vibration behavior during the startup process. The initial Young's modulus is set as E_0 (E_0 = 13.71 MPa). E_0 is multiplied by different coefficients to obtain five Young's moduli: 0.5 E_0, 0.75 E_0, E_0, 1.25 E_0, and 1.5 E_0. The obtained Young's modulus is substituted into finite element software for analysis.

Figure 19 shows the time-domain and frequency-domain diagrams of the frictional vibration during the startup process under five Young's moduli ranging from 0.5 E_0 to 1.5 E_0. From 0.5 E_0 to 1.5 E_0, the peak frequency increases from 1575.7 Hz to 2093.7 Hz, respectively, an increase of 32.9%, as shown in Figure 20. Similarly, in engineering design, choosing low-modulus materials to reduce the vibration frequency can also lead to a decrease in the load-bearing capacity. Therefore, a comprehensive consideration should be given between the vibration behavior and the load-bearing capacity to select the most suitable material.

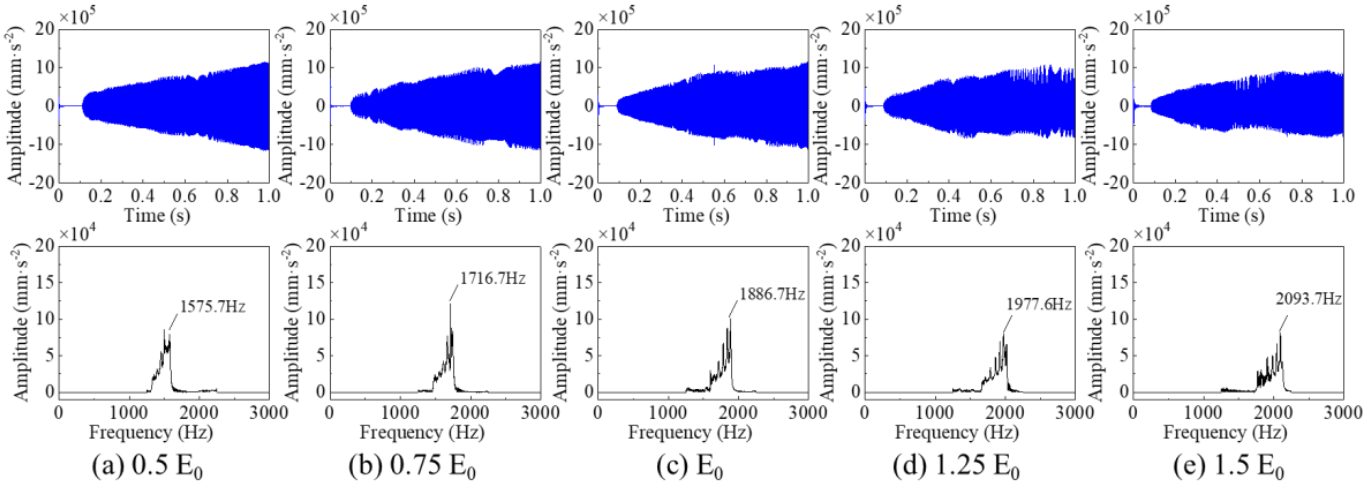

Figure 19. Time-domain and frequency-domain diagrams of startup process under different Young's moduli.

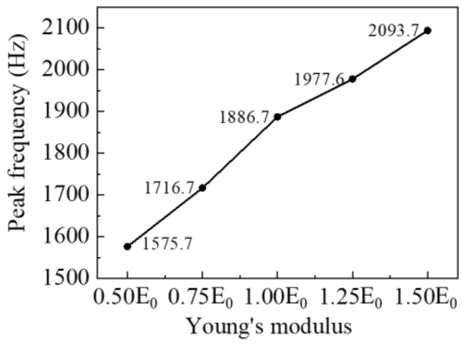

Figure 20. Peak frequency and downforce displacement of startup process under different Young's moduli.

The change in the Young's modulus mentioned earlier for the low-speed operating conditions indirectly affects the frictional vibration behavior, and the same is true during startup. During the startup process, the time-varying rotational speed and friction coefficient intensify the frictional vibration. As a result, the frictional vibration frequency increases with the increase in the Young's modulus. In addition, under the same Young's modulus, the friction-induced vibration frequency during the startup process is higher than that under low-speed operating conditions.

5. Conclusions

In this study, a finite element model of a friction pair composed of a copper ring and a rubber block is established. The real time-varying friction coefficient curve is substituted into the finite element model, and the frictional vibration behavior under special operating conditions (low-speed operating conditions and the startup process) is analyzed. The effects of the load, friction coefficient, and Young's modulus on the frictional vibration behavior under special operating conditions are studied, which have practical engineering significance to guide the material selection and material modification design of water-lubricated rubber bearing pads. The research results are as follows:

(1) The real and time-varying friction coefficients are included in the analysis, and a finite element model of the startup process is established, which can provide ideas for subsequent analyses.
(2) The increase in the load, friction coefficient, and Young's modulus all increase the frequency of frictional vibration. In engineering practice, comprehensive consideration should be given to selecting the most suitable material.

(3) Under low-speed operating conditions, the medium-high frequency vibration frequency disappears, and the frictional vibration behavior is excellent when the coefficient of friction drops below 0.1. In engineering practice, the friction coefficient should be reduced to within 0.1 to improve the friction performance.
(4) During the startup process, although the coefficient of friction is at a very low value, due to the variation in the rotational speed and friction coefficient over time, the medium-high frequency vibration frequency still occurs, and it does not disappear like in the low-speed operating condition. In future analysis work, the influence of factors such as the speed and the time-varying friction coefficient during the startup process should be considered.

Author Contributions: Conceptualization, G.Z.; methodology, Z.Z. and G.Z.; software, Z.Z. and P.L.; validation, Z.Z., L.D., and M.H.; formal analysis, Z.Z. and G.Z.; investigation, Z.Z. and P.L.; resources, G.Z.; data curation, Z.Z. and M.H.; writing—original draft preparation, Z.Z.; writing—review and editing, Z.Z. and G.Z.; visualization, L.D.; project administration, G.Z. All authors have read and agreed to the published version of the manuscript.

Funding: This study was supported by the Sichuan Science and Technology Program (No. 23ZDYF0425) and the Joint Fund of Equipment Pre-research and the Ministry of Education (8091B032209).

Institutional Review Board Statement: Not applicable.

Informed Consent Statement: Not applicable.

Data Availability Statement: Not applicable.

Conflicts of Interest: The authors declare no conflict of interest.

Abbreviations

Symbol	Symbol Meaning
M	mass matrix
P	internal force
F	external force
x	positional variable
α, β, γ	implicit integrating factor
f_0	actual friction coefficient
E_0	actual Young's modulus

References

1. Qiao, J.; Zhou, G.; Pu, W.; Li, R.; He, M. Coupling analysis of turbulent and mixed lubrication of water-lubricated rubber bearings. *Tribol. Int.* **2022**, *172*, 107644. [CrossRef]
2. Qu, C.; Wang, T.; Wang, Q.; Chen, S. A novel ternary interpenetrating polymer networks based on NBR/PU/EP with outstanding damping and tribological properties for water-lubricated bearings. *Tribol. Int.* **2022**, *167*, 107249. [CrossRef]
3. Wang, L.; Han, Y.; Tang, D.; Cai, J. Numerical and experimental investigations on the wear behavior of water-lubricated bearings with different materials. *Ind. Lubr. Tribol.* **2022**, *74*, 134–143. [CrossRef]
4. Zhou, G.; Qiao, J.; Pu, W.; Zhong, P. Analysis of mixed lubrication performance of water-lubricated rubber tilting pad journal bearing. *Tribol. Int.* **2022**, *169*, 107423. [CrossRef]
5. Zhou, G.; Wu, K.; Pu, W.; Li, P.; Han, Y. Tribological modification of hydrogenated nitrile rubber nanocomposites for water-lubricated bearing of ship stern shaft. *Wear* **2022**, *504–505*, 204432. [CrossRef]
6. Wu, C.; Chen, F.; Long, X. The self-excited vibration induced by friction of the shaft-hull coupled system with the water-lubricated rubber bearing and its stick-slip phenomenon. *Ocean Eng.* **2020**, *198*, 107002. [CrossRef]
7. Zhou, G.; Li, R.; Liao, D.; Yang, W.; Zhong, P. Lubrication structure design of water lubricated rubber thrust bearing with spiral groove for shaftless rim driven thruster. *Tribol. Int.* **2023**, *178*, 108098. [CrossRef]
8. Lin, C.-G.; Yang, Y.-N.; Chu, J.-L.; Sima, C.; Liu, P.; Qi, L.-B.; Zou, M.-S. Study on nonlinear dynamic characteristics of propulsion shafting under friction contact of stern bearings. *Tribol. Int.* **2023**, *183*, 108391. [CrossRef]
9. Cai, J.; Han, Y.; Xiang, G.; Wang, J.; Wang, L. Effects of wear and shaft-shape error defects on the tribo-dynamic response of water-lubricated bearings under propeller disturbance. *Phys. Fluids* **2022**, *34*, 077118. [CrossRef]
10. Cai, J.; Xiang, G.; Li, S.; Guo, J.; Wang, J.; Chen, S.; Yang, T. Mathematical modeling for nonlinear dynamic mixed friction behaviors of novel coupled bearing lubricated with low-viscosity fluid. *Phys. Fluids* **2022**, *34*, 093612. [CrossRef]

11. Chen, S.; Xiang, G.; Fillon, M.; Guo, J.; Wang, J.; Cai, J. On the tribo-dynamic behaviors during start-up of water lubricated bearing considering imperfect journal. *Tribol. Int.* **2022**, *174*, 107685. [CrossRef]
12. Xiang, G.; Yang, T.; Guo, J.; Wang, J.; Liu, B.; Chen, S. Optimization transient wear and contact performances of water-lubricated bearings under fluid-solid-thermal coupling condition using profile modification. *Wear* **2022**, *502–503*, 204379. [CrossRef]
13. Kinkaid, N.M.; O'Reilly, O.M.; Papadopoulos, P. Automotive disc brake squeal. *J. Sound Vib.* **2003**, *267*, 105–166. [CrossRef]
14. Pilipchuk, V.; Olejnik, P.; Awrejcewicz, J. Transient friction-induced vibrations in a 2-DOF model of brakes. *J. Sound Vib.* **2015**, *344*, 297–312. [CrossRef]
15. Lin, C.-G.; Zou, M.-S.; Sima, C.; Liu, S.-X.; Jiang, L.-W. Friction-induced vibration and noise of marine stern tube bearings considering perturbations of the stochastic rough surface. *Tribol. Int.* **2019**, *131*, 661–671. [CrossRef]
16. Spurr, R.T. A Theory of Brake Squeal. In Proceedings of the Institution of Mechanical Engineers: Automobile Division; Sage: Thousand Oaks, CA, USA, 1961; Volume 15, pp. 33–52.
17. Al-Zughaibi, A.I. Experimental and analytical investigations of friction at lubricant bearings in passive suspension systems. *Nonlinear Dyn.* **2018**, *94*, 1227–1242. [CrossRef]
18. Bhushan, B. Stick-Slip Induced Noise Generation in Water-Lubricated Compliant Rubber Bearings. *J. Lubr. Technol.* **1980**, *102*, 201–210. [CrossRef]
19. Krauter, A.I. Generation of Squeal/Chatter in Water-Lubricated Elastomeric Bearings. *J. Lubr. Technol.* **1981**, *103*, 406–412. [CrossRef]
20. Hongling, Q.; Chang, Y.; Hefa, Z.; Xufei, L.; Zhixiong, L.; Xiang, X. Experimental analysis on friction-induced vibration of water-lubricated bearings in a submarine propulsion system. *Ocean Eng.* **2020**, *203*, 107239. [CrossRef]
21. Zhang, Z.; Zhang, Z.; Huang, X.; Hua, H. Stability and transient dynamics of a propeller–shaft system as induced by nonlinear friction acting on bearing–shaft contact interface. *J. Sound Vib.* **2014**, *333*, 2608–2630. [CrossRef]
22. Simpson, T.A.; Ibrahim, R.A. Nonlinear Friction-induced vibration in Water-Lubricated Bearings. In Proceedings of the ASME 1995 Design Engineering Technical Conferences Collocated with the ASME 1995 15th International Computers in Engineering Conference and the ASME 1995 9th Annual Engineering Database Symposium, Boston, MA, USA, 17–20 September 1995.
23. Dong, C.; Yuan, C.; Bai, X.; Qin, H.; Yan, X. Investigating relationship between deformation behaviours and stick-slip phenomena of polymer material. *Wear* **2017**, *376–377*, 1333–1338. [CrossRef]
24. Liu, N.; Ouyang, H. Friction-induced vibration of a slider on an elastic disc spinning at variable speeds. *Nonlinear Dyn.* **2019**, *98*, 39–60. [CrossRef]
25. Kuang, F.; Zhou, X.; Liu, Z.; Huang, J.; Liu, X.; Qian, K.; Gryllias, K. Computer-vision-based research on friction vibration and coupling of frictional and torsional vibrations in water-lubricated bearing-shaft system. *Tribol. Int.* **2020**, *150*, 106336. [CrossRef]
26. Kuang, F.; Zhou, X.; Huang, J.; Wang, H.; Zheng, P. Machine-vision-based assessment of frictional vibration in water-lubricated rubber stern bearings. *Wear* **2019**, *426–427*, 760–769. [CrossRef]
27. Jin, Y.; Liu, Z.; Zhou, X. Theoretical, numerical, and experimental studies on friction vibration of marine water-lubricated bearing coupled with lateral vibration. *J. Mar. Sci. Technol.* **2019**, *25*, 298–311. [CrossRef]
28. Yang, J.; Liu, Z.; Liang, X.; Wang, J.; Cheng, Q. Research on Friction Vibration of Marine Water Lubricated Rubber Bearing. *Tribol. Online* **2018**, *13*, 108–118. [CrossRef]
29. Balaji, V.; Lenin, N.; Anand, P.; Rajesh, D.; Raja, V.B.; Palanikumar, K. Brake squeal analysis of disc brake. *Mater. Today Proc.* **2021**, *46*, 3824–3827. [CrossRef]
30. Chen, F.; Ouyang, H.; Wang, X. A new mechanism for friction-induced vibration and noise. *Friction* **2022**, *11*, 302–315. [CrossRef]
31. Ta, T.-N.; Horng, J.-H.; Hwang, Y.-L. Correlation Between Tribological and Vibration Behaviors in Sliding Lubricated Contacts. *J. Tribol.* **2022**, *144*, 111603. [CrossRef]
32. Zhou, G.; Li, P.; Liao, D.; Zhang, Y.; Zhong, P. The Friction-Induced Vibration of Water-Lubricated Rubber Bearings during the Shutdown Process. *Materials* **2020**, *13*, 5818. [CrossRef]
33. Newmark, N.M. A Method of Computation for Structural Dynamics. *Trans. Am. Soc. Civ. Eng.* **1962**, *127*, 1406–1433. [CrossRef]
34. Ryzhik, B. Friction-induced vibrations of squeal type due to transverse contraction in a flexible disk. *J. Sound Vib.* **2009**, *326*, 623–632. [CrossRef]
35. Brake, M.R.; Wickert, J.A. Frictional vibration transmission from a laterally moving surface to a traveling beam. *J. Sound Vib.* **2008**, *310*, 663–675. [CrossRef]